A spectral-element/Fourier smoothed profile method for large-eddy simulations of complex VIV problems

As Published: 10.1016/J.COMPFLUID.2018.06.022

Publisher: Elsevier BV

Persistent URL: https://hdl.handle.net/1721.1/135842

Version: Author's final manuscript: final author's manuscript post peer review, without publisher's formatting or copy editing

A Spectral-Element/Fourier Smoothed Profile Method for Large-Eddy Simulations of Complex VIV Problems

Zhicheng Wang[a,*], Michael S Triantafyllou[a], Yiannis Constantinides[b], George Em Karniadakis[c]

[a] *Massachusetts Institute of Technology, Cambridge, MA 02139 USA*
[b] *Chevron Energy Technology Company, Houston, TX 77002 USA*
[c] *Brown University, Providence, RI 02912 USA*

Abstract

An accurate, fast and robust spectral-element/Fourier smoothed profile method (SEF-SPM) for turbulent flow past 3D complex-geometry moving bluff-bodies is developed and analyzed in this paper. Based on the concept of momentum thickness δ_2, a new formula for determining the interface thickness parameter ξ is proposed. In order to overcome the numerical instability at high Reynolds number, the so-called Entropy Viscosity Method (EVM) is introduced in the framework of large-eddy simulation. To overcome resolution constraints pertaining to moving immersed bodies, the Coordinate Transformation Method (Mapping method) is incorporated in the current implementation. Moreover, a hybrid spectral-element method using mixed triangular and quadrilateral elements is employed in conjunction with Fourier discretization along the third direction to efficiently represent a body of revolution or a long-aspect ratio bluff-body like risers and cables. The combination of the above algorithms results in a robust method which we validate by several prototype flows, including flow past a stationary sphere at $200 \leq Re \leq 1\,000$, as well as turbulent flow past a stationary and moving cylinder at $80 \leq Re \leq 10\,000$. Finally, we apply the new method to simulate a self-excited rigidly moving dual-step cylinder and demonstrate that SEF-SPM is an efficient method for complex VIV problems.

Keywords: high-order methods, LES, entropy-viscosity, hybrid discretization, industrial flows

*Corresponding author
Email address: zhicheng@mit.edu (Zhicheng Wang)

1. Introduction

Prediction of the vortex induced vibration (VIV) of flexible risers is still a challenging task even by employing the state-of-the-art numerical methods on a supercomputer, e.g. in deep ocean oil exploration where the aspect ratio of the risers could be well over 1 000. This large aspect ratio requires a very large computational domain that direct numerical simulation (DNS) even at low Reynolds number seems computationally prohibitive. Furthermore, the complexity of the shape of the riser such as buoyancy modules (see figure 1) in conjunction with the high Reynolds number lead to additional difficulties in achieving accurate simulations.

Over the past several decades, the vast majority of the investigations of the VIV phenomena focused on uniform cylinders, see the comprehensive reviews in [1, 2, 3, 4, 5]. For the VIV of cylinder with complex shapes, especially for the flexible cylinder with large buoyancy module, only a few experimental investigations or semi-empirical simulations can be found in the literature, [6, 7, 8, 9]. To the best of our knowledge, no full-scale *three-dimensional* simulation results have been published for such cases. The main challenge in performing full-scale *three-dimensional* simulation of VIV of cylinder at high Reynolds number is that solving the 3D unsteady Navier-Stokes equations is computationally almost prohibitive. To meet this challenge, the spectral-element/Fourier (SEF) method that employs *two-dimensional* spectral element in one plane and Fourier expansion on the span-wise direction was proposed in [10] and subsequently was applied to DNS of VIV of flexible

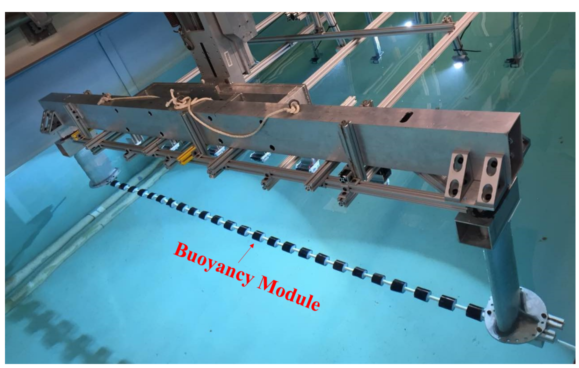

Figure 1: A model of the flexible riser with buoyancy modules used in our ongoing experiments at MIT. The small-diameter cylinder (white color) is the flexible riser and the large-diameter cylinders (black color) are the buoys. (Courtesy of Dixia Fan, MIT.)

risers in a number of studies [11, 12, 13, 14], where the Coordinate Transformation method (refer to Mapping method herein) was used to account for the unsteady boundary deformation. However, it is not straightforward to apply the Fourier method to a computational domain with varying geometric boundary along the span-wise direction, which is exactly the case of flow past a cylinder with buoyancy modules. To address this issue, we propose to combine SEF with the Smooth Profile Method (SEF-SPM). By utilizing the SPM indicator function, we can transform the non-uniformity of the geometric boundary into a smoothed indicator field that could be represented by Fourier series. The combination of SPM and Fourier method was first proposed by Nakayama and Yamamoto [15] to investigate fluid hydrodynamic interactions in colloidal suspensions and subsequently was applied to model flows containing charged particles [16, 17], Brownian particles [18] and for predicting the sedimentation of particles [19]. Subsequently, Luo et al. [20, 21] improved SPM by developing a high-order splitting scheme and implemented it on the 3D spectral-element code *Nektar*. Kang and Suh [22] proposed a one-stage SPM that potentially could save computational cost significantly by eliminating the additional pressure Poisson-equation solver. Also, Mohaghegh and Udaykumar [23, 24] showed that SPM is competitive against sharp interface approaches for particulate flows at moderate particle Reynolds numbers. Moreover, the application of SPM was extended to convective heat transfer by [25] and flow past a cylinder with random wall roughness in Zayernouri et al. [26].

The aforementioned applications of SPM have focused mostly on flows at small to moderate Reynolds number. The only SPM simulation of flow at high Reynolds number was reported in Luo et al. [27], who applied the 3D SPM spectral-element method to simulate waterjet flow at $Re \geq 2.3 \times 10^5$, using the Variational Multiscale Large-eddy simulation(VMS-LES) model for turbulence. It was reported that accurate and sustainable turbulent motions could be captured by SPM with VMS-LES approach but at high computational cost. As suggested in that paper, to use SPM in more industrial-complexity applications, further improvements of SPM to facilitate the *efficient* simulation of flow at high Reynolds number in complex-geometry, and more rigorous validations by modeling some prototype turbulent flows are required.

In the current paper, we will present a new implementation of SPM within the framework of SEF method together with the Mapping method that has been fully validated by modeling several VIV problems. We note that the overall method derives its efficiency from the Fourier discretization along the long direction that significantly accelerates the simulation. However, for flow past a moving body at high Reynolds number, in order to account for the moving boundary, SPM requires a very large computational domain with high resolution. To resolve this issue, we employ the Mapping method in conjunction with properly refined mesh, which together with the Fourier method (fast FFTs) lead to enhanced computational efficiency. With regards to modeling turbulence here we incorporate a new model, the so-called Entropy-viscosity method (EVM) that was originally proposed in Guermond et al. [28, 29] for hyperbolic conservation laws to stabilize simulations at insufficient resolution. EVM can be thought of as an Implicit Large-eddy simulation (ILES) approach and it was first validated for homogeneous isotropic turbulence in [30]. We have further developed the EVM by determining the only free parameter α by employing an analogy of the entropy-viscosity to the eddy viscosity of the Smagorinsky model. We have implemented our EVM in the SEF framework and have validated it systematically for fully developed turbulent pipe flow at Reynolds number up to 44 000 as well as for turbulent flows in a vibrating pipe, see Wang et al..

Lastly and perhaps most importantly, we propose here a new formula for determining the optimal value of the interface thickness parameter ξ of SPM. Previous works have shown that ξ has a great influence on the accuracy of the simulation results. Luo et al. [20] developed a rule based on the simulations of 2D Couette flow, which limits the value of the time step Δt. More recently, Mohaghegh and Udaykumar [23] proposed a formula for ξ that relates to both mesh size and the time step. The most effective value of ξ in these two rules depends on the discretization method and mesh, which is apparently not desirable in simulation of turbulent flow at high Reynolds number. To this end, we propose here a linear correlation between ξ and the *momentum thickness* δ_2 that is used often in boundary layer theory. We will demonstrate the accuracy of the new rule by simulating several prototype turbulent flows in subsequent sections.

The rest of the paper is organized as follows: in section 2 we will present the algorithms to solve the governing equations of incompressible flow and structure dynamics in the framework of the SEF method and the Mapping method. In the same section, we will also propose the new formula for determining ξ and relate it to the resolution requirements. In section 3, we will validate our method by simulating flow past a stationary sphere, a stationary cylinder and a self-excited rigidly moving cylinder at Reynolds number up to 10^4. In section 4, we will apply our method to predict the response of an elastically mounted dual-step cylinder subject to vortex shedding at $Re_d = 1\,000$, where d is the diameter of the small cylinder.

2. Computational methods

In this section, we will present the main steps of the SPM in the framework of spectral-element method following the work of [20]. In particular, our method combines elements from the work of [11] and [20].

2.1. Equations and numerical methods

We represent the immersed bluff-body by the following hyperbolic tangent function,

$$\phi(\mathbf{x}) = \frac{1}{2}[\tanh(\frac{-d(\mathbf{x})}{\xi}) + 1], \tag{1}$$

where $d(\mathbf{x})$ is the signed distance to surface of the immersed body, ξ is the interface thickness parameter, and $\phi(\mathbf{x})$ is a function of spatial coordinates $\mathbf{x}$; it is equal to 1 inside the riser, 0 in the fluid domain, and varies smoothly between 1 and 0 in the solid-fluid interfacial layer.

The fluid flow is governed by the incompressible Navier-Stokes equations:

$$\nabla \cdot \mathbf{u} = 0, \tag{2}$$

$$\frac{\partial \mathbf{u}}{\partial t} + \mathbf{u} \cdot \nabla \mathbf{u} = -\nabla p + (\nu + \nu_t)\nabla^2 \mathbf{u} + \mathbf{A}. \tag{3}$$

In equation 3, p and ν are pressure and kinematic viscosity, respectively. $\mathbf{A}$ is the additional acceleration introduced by the transformation of coordinate system; the detailed form of $\mathbf{A}$ can be found in [11].

In equation 3, ν_t is the entropy-viscosity, which was proposed in [28] and we further developed it here. It is calculated from the following formula in each element K at the collocation points ijm:

$$\nu_t|_K = \min\{\beta \|\mathbf{u}\|_{L^\infty(K)} \delta_K, \alpha \frac{\|R^K_{ijm}(\mathbf{u})\|_{L^\infty(K)}}{\|E^K_{ijm}(\mathbf{u}) - \bar{E}(\mathbf{u})\|_{L^\infty(\Omega)}} \delta_K^2\}, \tag{4}$$

where we use the maximum norm $L^\infty(K)$ over an element K or $L^\infty(\Omega)$ over the entire domain Ω. We define the various quantities as follows:

$$E^K_{ijm}(\mathbf{u}) = \frac{1}{2}(\|\mathbf{u}\|^K_{ijm} - \|\mathbf{u}\|_{L^\infty(\Omega)})^2, \quad \bar{E}(\mathbf{u}) = \frac{\int_\Omega E^K_{ijm}(\mathbf{u}) \cdot d\mathbf{X}}{\int_\Omega d\mathbf{X}} \tag{5}$$

$$R_{ijm}^K(\mathbf{u}) = \mathbf{u} \cdot (\frac{\partial \mathbf{u}}{\partial t} + \mathbf{u} \cdot \nabla \mathbf{u} + \nabla p - \frac{1}{Re} \nabla^2 \mathbf{u} - \mathbf{A})|_{ijm}^K, \tag{6}$$

where δ_K is the minimum distance between two quadrature points in element K.

Note that there are two parameters in equation 4: α and β. In our simulations, $\beta = 0.5$, which prevents the magnitude of ν_t exceeding the artificial viscosity of first-order upwind scheme [28]. However, the choice of α is somewhat depending on the type of flow. In our previous study on decaying homogeneous isotropic turbulence, we have found $\alpha = 0.5$ could give correct spectrum and Taylor scale Reynolds number, see [31]. For internal flow, for instance turbulent pipe flow, our simulations showed that α should be tuned to as small as $\alpha = 0.005$. Here we note that *for all the simulations in this paper, unless otherwise stated, the EVM parameter α is equal to 0.5.* Furthermore, in the current simulations the entropy viscosity is always smaller than the artificial viscosity corresponding to a first-order upwind-scheme.

Given $(\mathbf{u}^n, p^n, \phi)$, we first explicitly integrate the nonlinear term $N(\mathbf{u}) = \mathbf{u} \cdot \nabla \mathbf{u}$ and $\mathbf{A}$ as follows:

$$\frac{\hat{\mathbf{u}} - \sum_{q=0}^{J-1} \alpha_q \mathbf{u}^{n-q}}{\Delta t} = \sum_{q=0}^{J-1} \beta_q [-N(\mathbf{u}) + \mathbf{A}]^{n-q}, \tag{7}$$

where α_q and β_q are the coefficients of the stiffly-stable integration scheme we employ with $J = 2$ the integration order. Note that the prescribed velocity boundary condition is also updated at this stage as follows,

$$\mathbf{u}^{n+1} = -\mathbf{v} \tag{8}$$

where $\mathbf{v}$ is the velocity of the reference frame. In the next stage we solve the intermediate pressure field,

$$\nabla^2 p^* = \nabla \cdot (\frac{\hat{\mathbf{u}}}{\Delta t}), \tag{9}$$

with the following pressure boundary condition at all the velocity Dirichlet boundaries,

$$\frac{\partial p^*}{\partial \mathbf{n}} = \sum_{q=0}^{J-1} [-N(\mathbf{u}) + \mathbf{A} - \nu \nabla \times (\nabla \times \mathbf{u})]^{n-q} \cdot \mathbf{n}, \tag{10}$$

where $\mathbf{n}$ is the unit outward normal vector at the boundaries.

In the third stage of the method we compute the intermediate velocity $\mathbf{u}^*$,

$$(\nabla^2 - \frac{\gamma_0}{\nu\Delta t})\mathbf{u}^* = -\frac{\hat{\mathbf{u}}}{\nu\Delta t} - \frac{\nu_t}{\nu}\nabla^2\mathbf{u}^{*,n+1}, \tag{11}$$

where γ_0 is the scaled coefficient of the stiffly-stabled scheme, see [32, 20]. $\mathbf{u}^{*,n+1} = \sum_{q=0}^{J-1}\beta_q\mathbf{u}^{n-q}$ represents the J^{th} order explicit approximation of $\mathbf{u}^{n+1}$.

If this is the first iteration, then the fourth stage to obtain the immersed body velocity is as follows,

$$\mathbf{u}_p = \phi\mathbf{V}_s, \tag{12}$$

where $\mathbf{V}_s$ is the translational velocity of the immersed bluff-body in the non-inertial coordinate frame. If SPM is coupled with the Mapping method, then $\mathbf{V}_s$ is always $zero$!

Next, we solve the extra pressure field p_p due to the immersed bluff-body,

$$\nabla^2 p_p = \nabla\cdot(\frac{\gamma_0\phi(\mathbf{u}_p - \mathbf{u}^*)}{\Delta t}). \tag{13}$$

Here the following is used as the boundary conditions for p_p at any velocity Dirichlet boundary,

$$\frac{\partial p_p}{\partial \mathbf{n}} = \frac{\gamma_0\phi(\mathbf{u}_p - \mathbf{u}^*)}{\Delta t}\cdot\mathbf{n}. \tag{14}$$

Finally, the total velocity field is updated as follows,

$$\frac{\gamma_0\mathbf{u}^{n+1} - \gamma_0\mathbf{u}^*}{\Delta t} = \frac{\gamma_0\phi(\mathbf{u}_p - \mathbf{u}^*)}{\Delta t} - \nabla p_p. \tag{15}$$

Note that through equations (7-15), the no-slip and no-penetration boundary conditions are fulfilled automatically, see [20].

Since we are interested in simulating VIV, we also specify the structure response governed by a linear tensioned-beam dynamic equation:

$$\frac{\partial^2 y}{\partial t^2} - \omega_c^2\frac{\partial^2 y}{\partial z^2} + \omega_b^2\frac{\partial^4 y}{\partial z^4} = \frac{F}{m}. \tag{16}$$

In equation 16, y and m represent displacement and mass on each cross-section of the immersed body, respectively; ω_b and ω_c are beam and cable phase velocities, respectively. F is the hydrodynamic force exerted on the cross-section of the immersed body, and its value at step $n+1$ is defined as:

$$F^{n+1} = \int_\Omega [\frac{\phi(\mathbf{u}^* - \mathbf{u}_p)}{\Delta t} - \frac{\Delta p_p}{\gamma_0}]\, d\mathbf{x}, \tag{17}$$

where the subscript Ω represents the entire computational domain. It is noteworthy that equation 17 provides a very convenient way to obtain the hydrodynamic forces exerted on the immersed bluff-body, as this equation only involves a volume integral. We employ the Newmark integration scheme to solve the structure dynamic equation 16, the details of which could be found in [11, 12].

The numerical schemes listed in equations (2-17) were implemented in the parallel code *Nektar* that employs Jacobi polynomial-based expansion basis in (x, y)-plane and Fourier expansion in the homogeneous direction (z direction); more details can be found in [33].

2.2. The interface thickness parameter ξ and grid resolution

SPM simulation results are quite sensitive to the interface thickness parameter ξ. Since the first paper on SPM by Nakayama and Yamamoto [15], there have been several studies on the most effective value of ξ. Nakayama and Yamamoto [15] obtained the correct value of drag coefficient by choosing an integer factor of the grid size for ξ in their simulation of creeping flow at $Re \leq 20$; Kang and Suh [22] and Romanó and Kuhlmann [25] adopted this approach in their SPM simulations. Luo et al. [20] extended the application of SPM to moderate Re (a few hundred) flows by using a semi-implicit high order splitting scheme and implementing it in the context of 3D spectral-element discretization. It was found that for the best accuracy, the following equation should be followed,

$$2.76\sqrt{\nu \Delta t} \approx 2.07\xi, \tag{18}$$

where the left-hand-side term represents the Stokes layer thickness, the right-hand-side term denotes the effective interface layer thickness, and Δt is the time step. This formula works well for flow at $Re \leq 500$, but the drawback is it implies that ξ is dependent on Δt, which is not desirable in numerical simulations. More recently, Mohaghegh and Udaykumar [23] proposed another correlation to tune ξ and Δt, which is

$$\xi = \kappa \Delta x (0.20 + 1.7 Re^{-0.4})(10\, CFL)^{(0.65+0.1/Re)} Re^{-0.11}, \tag{19}$$

where κ is a factor that is equal to 6 in *three-dimensional* simulation and 3 in *two-dimensional* simulation, Δx is the grid size and CFL is the advection time step limit. The above formula seems to work well for the cases in [23, 24], however, this formula is still mesh size or time step dependent.

Here, based on our numerical experiments of SEF-SPM simulation of flow past a bluff-body (sphere and cylinder) at moderate and high Reynolds number ($80 \leq Re \leq 10^4$), we propose the following rule to determine the value ξ,

$$\xi = \epsilon\, \delta_2, \tag{20}$$

where δ_2 represents the momentum thickness and ϵ is a constant factor. Assuming that the curvature effects are not important, at the location of the sphere or cylinder where $x = \frac{\pi D}{4}$ (measured from the front stagnation point), Schlichting and Gersten [34] gives an estimate of the the smallest value of δ_2 as follows,

$$\delta_2 = \frac{0.664}{\sqrt{0.25\, Re \cdot \pi}}. \tag{21}$$

Surprisingly, similar to factor κ in the correlation of [23], we have found the value of ϵ for *two-dimensional* simulation should be half of that of *three-dimensional* simulation; specifically, $\epsilon = 0.2$ for *two-dimensional* simulation and $\epsilon = 0.4$ for *three-dimensional* simulation give rise to accurate results.

Having decided the value of ξ, the grid resolution could also be determined. We note that SEF-SPM requires the indicator field ϕ to be sufficiently smooth. To this end, we found that if there is at least *one* supporting points (quadrature points) within the inter-facial region, the simulation is accurate and stable. For our SEF-SPM, we found the resolution requirement in (x, y)-plane is stricter than that in z direction. Specifically, the following two rules work well for our simulations of flow past a sphere and cylinder,

$$\frac{L_E}{M} \leq \xi, \tag{22}$$

$$\frac{L_z}{P} \leq 6\, \xi, \tag{23}$$

where L_E is the length of the element edge, L_z is the length of the domain in z direction, M is the order of spectral-element polynomial, and P is the number of Fourier planes, see figure 2.

3. Validation by a stationary and moving bluff-body

In this section we will validate systematically SEF-SPM by simulating turbulent flow past bluff bodies and compare against available experimental results and direct numerical simulations (DNS).

3.1. Flow past a stationary sphere

To demonstrate that the SEF-SPM is able to produce accurate results of flow past a $3D$ shape immersed body, we have performed systematic simulations of flow past a stationary sphere at $Re = 200, 300$ and $1\,000$. The numerical study of [35] shows that wake flow behind a stationary sphere is steady and axisymmetric at $Re = 200$, non-axisymmetric with steady 'double-thread' like streamwise vortices at $Re = 300$, and leads to unsteady shedding vortex at $Re = 1\,000$, i.e., the three values of Re correspond to three different wake patterns. Hence, this is a good testbed to validate the SEF-SPM on modeling flow past a 3D complex immersed-body.

The mesh has 2676 conforming elements: 62 triangles and 2614 quadrangles. The overall dimensions of the computational domain in terms of the diameter of the sphere d are: $[-6.5\,d, 25\,d] \times [-10\,d, 10\,d]$ with the center of the sphere located at $(0, 0)$, while the length on span-wise direction (z) is $8\,d$. Figure 2(a) shows part of a *two*-dimensional section ($x - y$ plane) of the computational domain and the corresponding mesh. Note that, as shown in the lower panel of figure 2(a), on one hand, in order to resolve the immersed body within the square $[-0.55\,d, 0.55\,d] \times [-0.55\,d, 0.55\,d]$ that contains the sphere, a structured mesh consisting of 34×34 quadrilateral elements was used; on the other hand, to maintain an overall low number of elements triangles are used in order to transition from small quadrilateral elements to large quadrilateral elements. In the refined square, the grid resolution is $L_E/M \leq 0.011d$ in $x - y$ plane and $L_z/P \leq 0.0625d$ on z direction. Concerning the boundary conditions, uniform velocity $\mathbf{u} = (1, 0, 0)$ is prescribed at the inlet boundary, periodicity is imposed at all side boundaries, while at the outlet boundary, $\frac{\partial \mathbf{u}}{\partial n} = 0$ for velocity and $p = 0$ for pressure are employed.

We have performed a dozen of simulations to verify the correlation between ξ and δ_2 proposed in equation 20. Moreover, we examined the sensitivity of SEF-SPM results to mesh size and time step. Table 1 shows the values of M, P and Δt used in each computation and the simulation results. Values of the drag coefficient C_D and Strouhal number St from literature

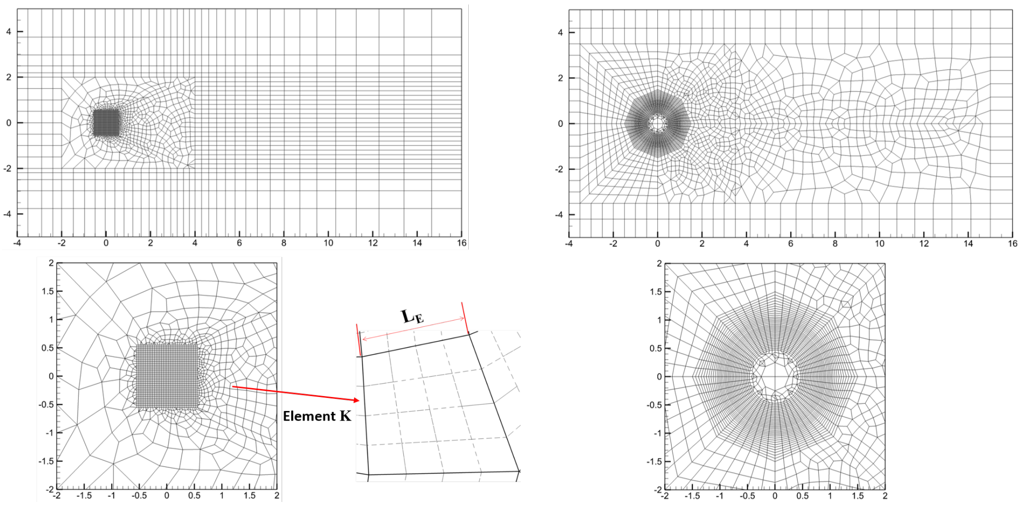

(a) (b)

Figure 2: Examples of computational domains and hybrid meshes (triangles and quadrangles) for SEF-SPM simulations of flows past a sphere or a cylinder: (a) MESH1, a structured mesh is embedded inside an unstructured hybrid mesh used for cases that the immersed body is stationary and the Reynolds number is relatively low; (b) MESH2, body-aligned mesh for case that the Reynolds number is high or the immersed body is moving. The figures on the lower panel are enlargements of the area that contains the immersed body. The sketch defines the length in equations 22.

are also presented in table 1. We see that the result of the SEF-SPM simulation is sensitive to ξ, but as long as ξ is close to the most effective value obtained by equation 20, it leads to accurate results for the drag coefficient. SEF-SPM under-predicts the St by at most 8% compared with DNS when ξ has the optimal value. It is noteworthy that the under prediction of the vortex shedding frequency is not rare for a diffusive interface method, see Romanó and Kuhlmann [25]. Another observation from table 1 is that there is very minor quantitative variation as the time step Δt is decreased, provided the ξ follows equation 20. Furthermore, from the table, it can be seen that the variation of the simulation results due to mesh refinement both in $(x-y)$ plane and z direction is negligible, which means our SEF-SPM is not sensitive to the mesh size under the condition that the resolution fulfills the requirement imposed by equation 22.

Now let us turn to the wake structures of flow past a sphere at $Re = 300$ and $Re = 1\,000$, both of which are shown in figure 3. Here the vortices are visualized by the Q-criterion. In figure 3(a), we see that there is an

Table 1: Flow past a stationary sphere: Mesh resolution, interface thickness and pressure and force coefficients. δ_2 represents the momentum thickness, $C_D = \frac{F_D}{0.5\,U_\infty^2\,A_D}$ the drag coefficient, $St = \frac{f_D\,D}{U_\infty}$ the Strouhal number, where F_D is the drag force, A_D is the projection area of the sphere, f_D is the frequency of the wake velocity on y direction, and $C_{D,F}$, $C_{D,P}$ correspond to the first and second terms on the right-hand-side of equation 17, respectively. P is the number of Fourier planes, M is the order of spectral-element polynomial.

Re	Method	Mesh resolution	δ_2	ξ	$C_{D,F}$	$C_{D,P}$	C_D	St
200	DNS	Johnson and Patel [36]	0.053	-	-	-	0.8	-
	SEF-SPM	$P = 128,\ M = 3,\ \Delta t = 0.005$		0.02	0.589	0.146	0.735	-
		$P = 128,\ M = 3,\ \Delta t = 0.005$		$\underline{0.0212}$	0.628	0.164	0.792	-
		$P = 128,\ M = 3,\ \Delta t = 0.003$		$\underline{0.0212}$	0.632	0.165	0.797	-
		$P = 128,\ M = 3,\ \Delta t = 0.005$		0.03	0.656	0.169	0.825	-
300	DNS	[35]	0.043	-	-	-	0.67	0.136
	SEF-SPM	$P = 128,\ M = 3,\ \Delta t = 0.005$		0.03	0.598	0.147	0.745	0.123
		$P = 128,\ M = 3,\ \Delta t = 0.005$		$\underline{0.0172}$	0.527	0.127	0.654	0.125
		$P = 128,\ M = 4,\ \Delta t = 0.003$		$\underline{0.0172}$	0.539	0.136	0.676	0.125
		$P = 256,\ M = 3,\ \Delta t = 0.005$		$\underline{0.0172}$	0.531	0.132	0.663	0.126
		$P = 128,\ M = 4,\ \Delta t = 0.003$		0.015	0.504	0.138	0.640	0.126
		$P = 128,\ M = 4,\ \Delta t = 0.003$		0.01	0.481	0.122	0.603	0.126
1000	DNS	[35]	0.024	-	-	-	0.48	0.195
	SEF-SPM	$P = 128,\ M = 4,\ \Delta t = 0.002$		$\underline{0.011}$	0.373	0.094	0.467	0.185
		$P = 256,\ M = 4,\ \Delta t = 0.002$		$\underline{0.011}$	0.369	0.110	0.479	0.181

unsteady non-axisymmetric hairpin vortex detached from the sphere for flow at $Re = 300$. When the Reynolds number is increased to $1\,000$, as shown in figure 3(b), the shear layer is rolled-up and more small scale flow structures appear. The visualization of the vortices in figure 3(a) is very similar to the experimental images in Johnson and Patel [36], while that in figure 3(b) resembles the DNS result of Yang and Balaras [37], suggesting that SEF-SPM can accurately model flow past non-uniform 3D immersed-bodies.

3.2. Flow past a stationary cylinder

Here we validate the SEF-SPM for unsteady flow past a stationary cylinder. We have carried out both *two-dimensional* simulations of laminar flow wake and *three-dimensional* simulations of turbulent wake for Reynolds number up to 10^4. For all the simulations in this section, the computational domain is the same: $[-6.5\,d, 23.5\,d] \times [-10\,d, 10\,d]$ with the center of the cylinder located at $(0, 0)$. Note that we have used two types of mesh: for the *two-dimensional* simulation at $Re \leq 500$ as well as the *three-dimensional*

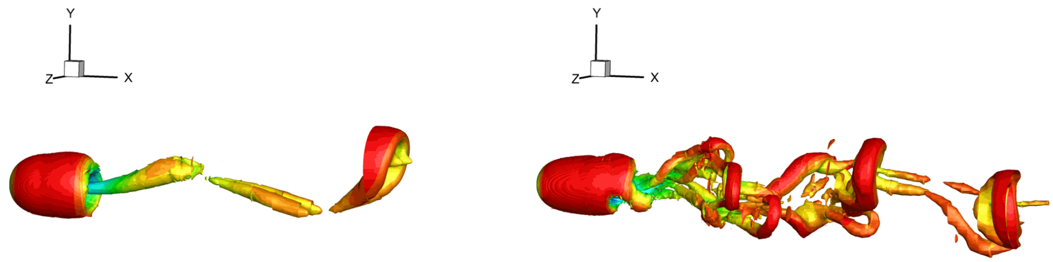

(a) $Re = 300$ (b) $Re = 1\,000$

Figure 3: Flow past a sphere: instantaneous structure of hairpin vortices visualized by iso-surfaces of $Q = 0.1$. The iso-surfaces are colored by pressure p: red, $p > 0$; blue, $p < 0$. The pattern of (a) resembles the visualization presented in figure 33 in [36], while the pattern in (b) resembles figure 3 in [37].

simulation at $Re = 1\,000$ the mesh (MESH1, see the caption of figure 2) includes a structured sub-mesh that contains the cylinder, as shown in figure 2(a). For the $3D$ simulations at $Re = 4\,000$ and $Re = 10\,000$, the mesh (MESH2, see the caption of figure 2) is generated so that the mesh boundaries are aligned with the surface of the cylinder but are not necessary body-fitted, as shown in figure 2 (b). MESH1 consists of 4813 elements: 200 triangles and 4613 quadrangles, while MESH2 consists of 3008 elements: 56 triangles and 2952 quadrangles. Using a meshing approach as in MESH2 we can greatly reduce the number of elements without involving adaptive mesh refinement technology. For the *three-dimensional* simulations at $Re = 1\,000$, $Re = 4\,000$ and $Re = 10\,000$, 32, 64 and 128 Fourier planes are used, respectively. The boundary conditions are the same as those of flow past a sphere.

Table 2 presents the comparison between SEF-SPM solutions and those in the literature, for values of ξ obtained from equation 20. In general, we can see that SEF-SPM solutions match the corresponding reference values very well. Concerning the coefficients in table 2, the agreement between the current $2D$ SEF-SPM solution and our own DNS is almost perfect. The difference for drag coefficient C_D between the current simulation from that of [38] is due to the effect of domain size. For $3D$ turbulent flow, the current SEF-SPM solutions are consistent with those in the literature. At $Re = 1\,000$ and $Re = 4\,000$, the difference among current SEF-SPM solutions and those of DNS or LES is less than 4% for all the coefficients. However, for the length of the re-circulation bubble L_r at $Re = 10\,000$, the difference is over 13%, and this may be due to the relatively small size of our domain as well as the effect of parameter α of EVM , see the magnitude of L_r at different α in table A.4 in Appendix A.

Table 2: Flow past a 2D and 3D stationary cylinder at different Re numbers: pressure ($-C_P = \frac{p_\infty - p}{0.5\, U_\infty}$) and drag ($C_D$) coefficients, Strouhal number (St), and length of the recirculation bubble (L_r). 2D and 3D DNS were performed in current study on the same mesh as SEF-SPM.

Re	**Study**	$\boldsymbol{\delta_2}$	$\boldsymbol{\xi}$	$\boldsymbol{C_D}$	$\boldsymbol{-C_P}$	$\boldsymbol{St}$	$\boldsymbol{L_r}$
80	2D DNS Henderson [38]	0.084	-	**1.341**	**0.676**	**0.154**	-
	2D DNS		-	1.452	0.657	0.156	1.65
	2D SEF-SPM		0.0168	1.479	0.672	0.165	1.65
200	DNS Henderson [38]	0.053	-	**1.341**	**0.999**	**0.197**	-
	2D DNS		-	1.403	0.979	0.201	0.85
	2D SEF-SPM		0.0106	1.416	1.014	0.201	0.82
500	2D DNS Henderson [38]	0.034	-	**1.445**	-	**0.225**	-
	2D DNS		-	1.494	1.408	0.228	0.51
	2D SEF-SPM		0.007	1.502	1.433	0.224	0.50
1 000	3D DNS Evangelinos and Karniadakis [12]	0.024	-	**1.019**	**0.843**	**0.202**	-
	3D DNS		-	1.106	0.86	0.204	1.42
	3D SEF-SPM		0.01	1.103	0.84	0.201	1.45
4 000	3D DNS Dong et al. [39]	0.012	-	-	**0.93**	**0.208**	**1.36**
	3D LES Kravchenko and Moin [40]		-	**1.04**	**0.94**	**0.207**	**1.40**
	3D SEF-SPM		0.005	1.08	0.92	0.206	1.43
$\mathbf{10^4}$	3D DNS Dong et al. [39]	0.008	-	**1.143**	**1.129**	**0.203**	**0.82**
	3D SEF-SPM		0.003	1.151	1.024	0.197	0.98

Next let us examine the pressure coefficient C_p along the surface of the cylinder. Figures 4 (a) and (b) compare the SEF-SPM solution of C_p with those of DNS and experiments at $Re = 500$ and $Re = 4\,000$. We observe that the SEF-SPM solution agrees with the corresponding DNS and experiments very well. Figure 5 shows the comparison of the mean stream-wise velocity $\frac{<u>}{U_\infty}$ along the center line ($y/d = 0$) in the cylinder wake. Again, we could observe that the SEF-SPM solution matches well with that of DNS at $Re = 500$ and the PIV experiments at $Re = 3\,900$. Note that the slight shift between SEF-SPM solution of $\frac{<u>}{U_\infty}$ and that of PIV indicates that the PIV experiment at $Re = 3\,900$ captured a longer recirculation bubble that is $L_r = 1.67$, see [41]; this is due to the relatively small domain size in our simulation.

Figure 6 compares the $\frac{<u>}{U_\infty}$ among SEF-SPM solution, experimental measurements by [41] and Lourenco and Shih at three locations ($x/d = 1.06, 1.54, 2.02$) in the near wake. We can see that the SEF-SPM solution agrees well with the measurements of [41] for $\frac{<u>}{U_\infty}$ at all three locations.

Figure 7 presents the cross-flow spectra at the near wake location $x/d = 0.54, y/d = 0.65$ and further downstream location $x/d = 3.14, y/d = 0.4$. The spectra of DNS of [39] at the same locations are plotted together. Note that the current calculation of the spectra is based on averaging along the span-wise direction. The overall agreement between the current simulation and DNS is good, indicating that SEF-SPM could predict all the large scale motion at both locations. However, due to the dissipation by using $\alpha = 0.5$, SEF-SPM yields a faster decay at the inertial subrange of the spectrum as expected. We examine the effect of α on the spectra at higher Reynolds number in Appendix A.

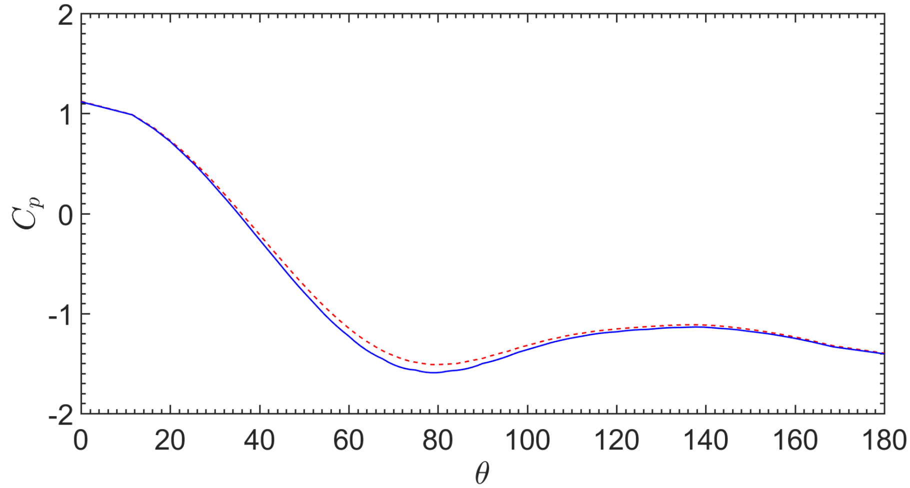

(a) $Re = 500$

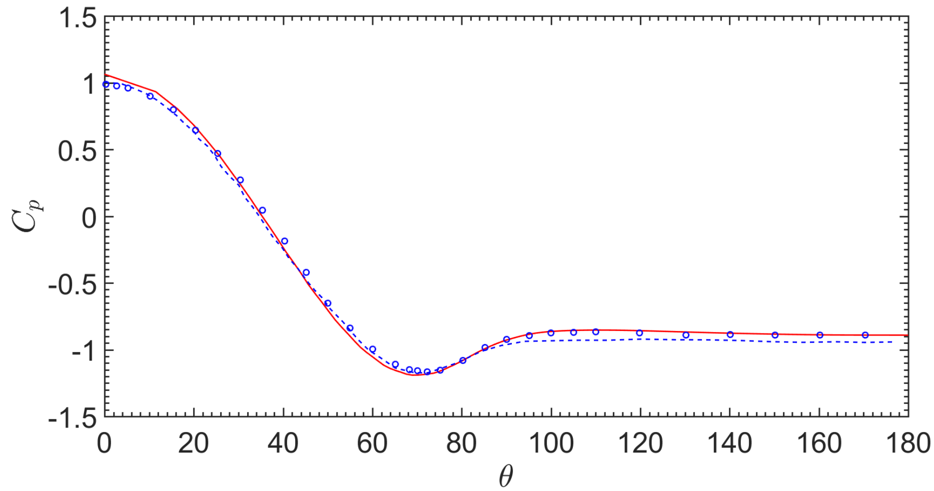

(b) $Re = 4\,000$

Figure 4: Flow past a cylinder: pressure coefficients along the surface of the cylinder. (a) $Re = 500$, 2D flow: blue solid line, current DNS; red dashed line, SEF-SPM. (b) $Re = 4000$, 3D flow: red line, SEF-SPM; blue circles, experimental measurements of Norberg [43] at $Re = 4\,020$; blue dashed line, LES of Kravchenko and Moin [40].

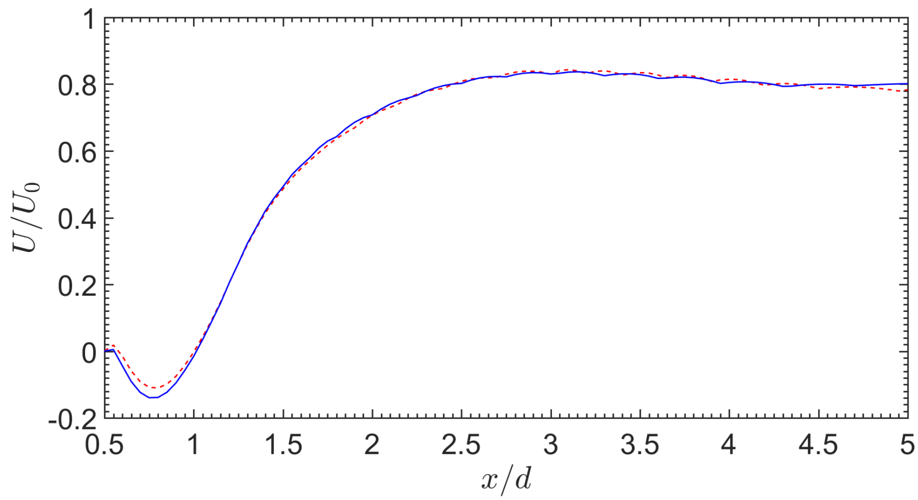

(a) $Re = 500$

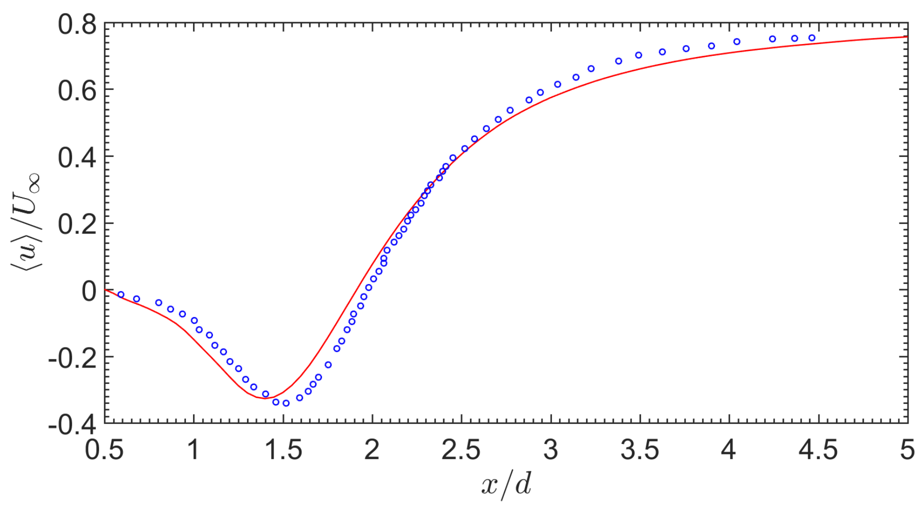

(b) $Re = 4\,000$

Figure 5: Flow past a stationary cylinder: mean stream-wise velocity in the wake of the cylinder. (a): blue solid line, current DNS; red dashed line, SEF-SPM solution. (b): red line, SEF-SPM solution; blue circles, PIV measurements at $Re = 3\,900$ of Parnaudeau et al. [41].

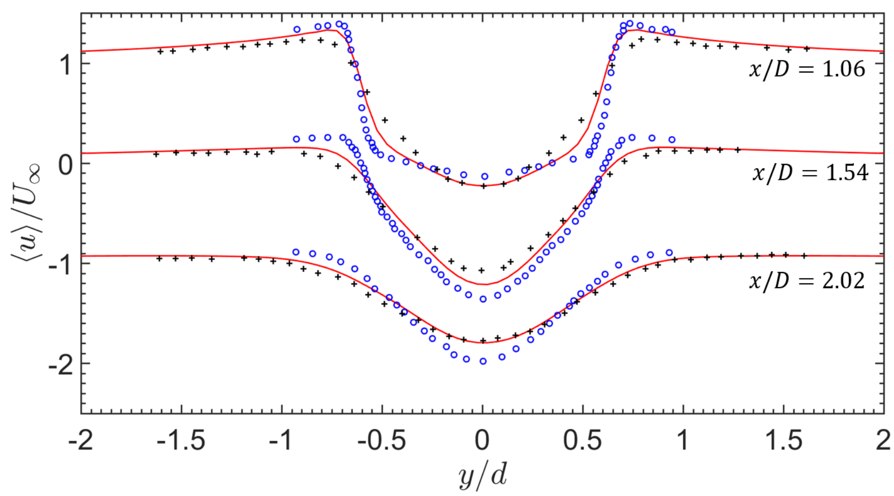

Figure 6: Flow past a stationary cylinder: mean stream-wise velocity at three locations in the wake of the cylinder at $Re = 4\,000$. Red line, SEF-SPM solution; blue circles, PIV measurements at $Re = 3\,900$ of Parnaudeau et al. [41]; black crosses, measurements by Lourenco and Shih.

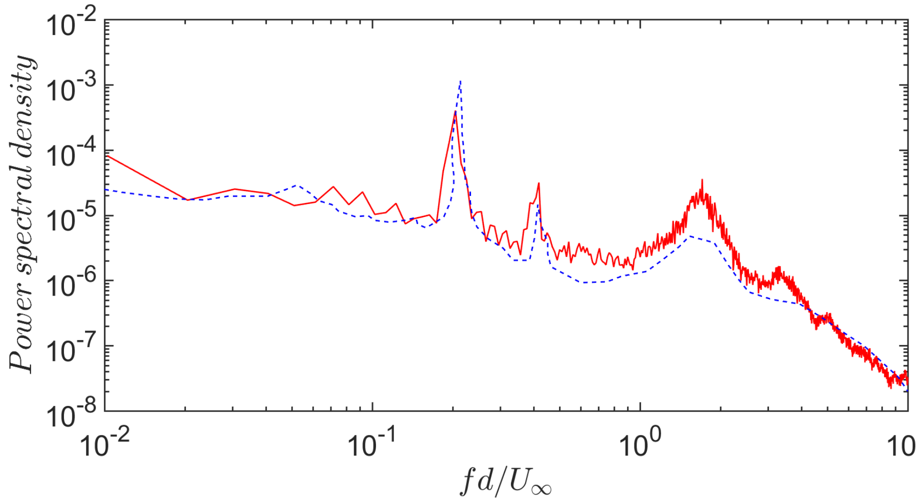

(a)

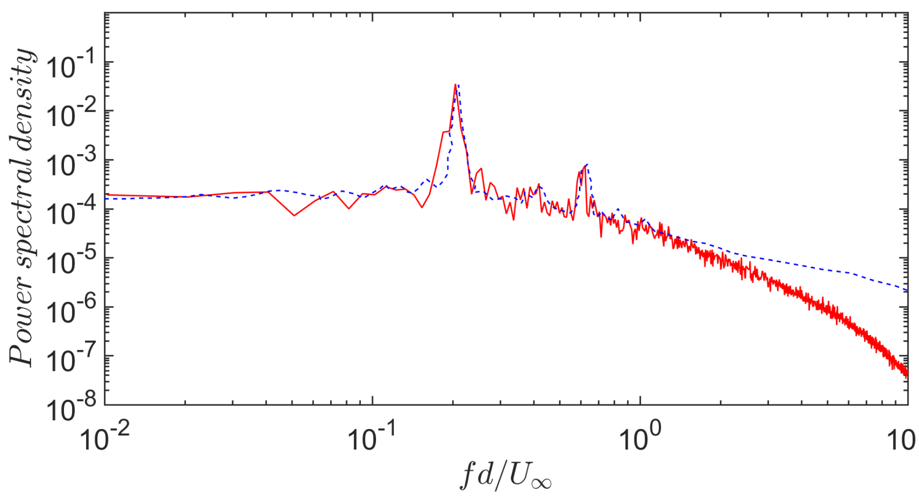

(b)

Figure 7: Flow past a stationary cylinder: cross-flow velocity spectra at $Re = 4\,000$. (a) point $x = 0.54$ and $y = 0.65$; (b) point $x = 3.14$ and $y = 0.4$. Red lines are SEF-SPM solutions, blue dashed lines are DNS of Dong et al. [39].

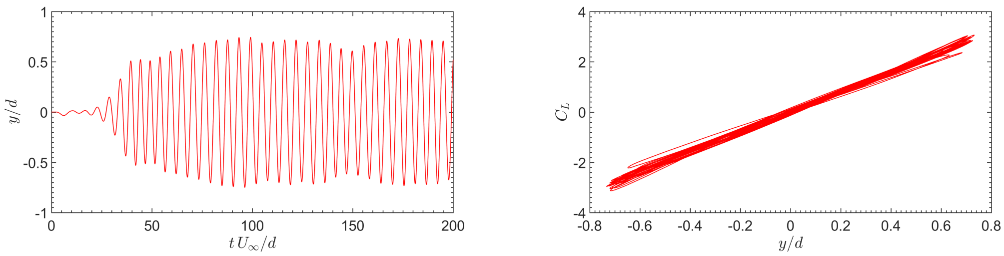

(a) (b)

Figure 8: Flow past a self-excited rigidly moving cylinder at $Re = 1\,000$: (a) cross flow displacement versus time, (b) span-averaged lift coefficient versus cross-flow displacement. It is noteworthy that both figures resemble figure 3(a) and figure 3(b) in [12].

3.3. Rigidly moving cylinder

Here, we will validate SEF-SPM by simulation of flow past a self-excited rigidly moving cylinder at $Re_d = 1\,000$. The computational domain along the x direction is the same as that of stationary cylinder, but along the y direction it is expanded to $[-20d, 20d]$. The domain consists of 3072 elements: 56 triangles and 3016 quadrangles. The mesh is similar to MESH2 (see the caption of figure 2)). It is worth mentioning that here SEF-SPM employs the Mapping method that can account for boundary deformations on a fixed mesh. The parameters of the structure dynamic equation 16 are the same as those used in [12]: $m = 2$, $\omega_c = 0.$ and $\omega_b = 2\pi\, f_N$, where $f_N = 0.238$ is the natural frequency of the rigid cylinder. Figure 8(a) shows the harmonic motion induced by the periodic vortex shedding. We observe that the SEF-SPM simulation produces a maximum amplitude response $y/d \approx 0.73$ that is slightly smaller than the corresponding value $y/d \approx 0.74$ in [12]. Same as that in [12], our simulation also shows that the motion is synchronized (lock-in) with the span-averaged lift coefficient as shown in figure 8(b). As regards the response frequency, the SEF-SPM result of the non-dimensional structure frequency (obtained from the spectrum of cross-flow motion) is $f\,d/U_\infty = 0.186$ and vortex shedding frequency (obtained from cross-flow velocity in the wake at $x/d = 3, y/d = 0.$) is $f\,d/U_\infty = 0.192$, both of which are less than 6% smaller compared with those of [12].

4. Applications to flow past a dual-step cylinder

Having validated the SEF-SPM both for the stationary and moving immersed-bodies, here we apply it to simulate flow past a stationary and rigidly moving dual-step cylinder, which is comprised of a large diameter cylinder (D) at the midspan of a small cylinder (d). We chose this case given existing PIV measurements at $1\,000 \leq Re_d \leq 2\,500$ published in [44, 45, 46] as well as the numerical study at $Re_d = 150$ presented in [47]. The measurements revealed a strong dependence of the vortex shedding on the aspect ratio L/D, diameter ratio D/d and Reynolds number, where L is the length of the large cylinder along the span-wise direction. Moreover, the measurements also revealed two distinct vortex shedding frequencies, one due to the large cylinder and the other one due to the small cylinder. However, in the aforementioned studies, the dual-step cylinder was stationary and no detailed information of the hydrodynamic force was presented. To the best of our knowledge, the VIV characteristics of the dual-step cylinder, which is a simplified model of the buoyancy-module that is often employed in the deep-sea oil industry, has not been investigated thoroughly. Hence, the simulation of VIV of dual-step cylinder we present here will not only provide a further validation of the SEF-SPM but will also provide new physical insight into the vibration of the buoyancy-module in [8, 9].

4.1. Stationary dual-step cylinder

The experimental and simulation models are shown in figure 9. Note that various models with different L/D, D/d and Reynolds number were tested in experiments but in our simulation the focus is on a model corresponding to $L/D = 1$, $D/d = 2$ and $Re_d = 1\,000$. As regards the discontinuity in diameter, one notable difference between the experimental model and simulation model is that the radius of our simulation model (r) is varied gradually from the smaller one to larger one as follows,

$$r = \frac{d}{2} + \frac{D-d}{2}[\tanh(\,\mathrm{sign}(z')\frac{z-Z'}{\delta}) + 1], \tag{24}$$

where z is the coordinate along the span-wise direction, with the parameter $\delta = 0.2\,d$ controlling the steepness of the r profile; sign$(\cdot)$ is the *sign* function, z' and Z' are defined as $z' = z - \frac{L_z}{2}$ and $Z' = \frac{L_z - \mathrm{sign}(z')L}{2}$, respectively. A smoothed variation of the radius is required for SEF-SPM due to the Fourier discretization along the span. However, we will demonstrate later that the

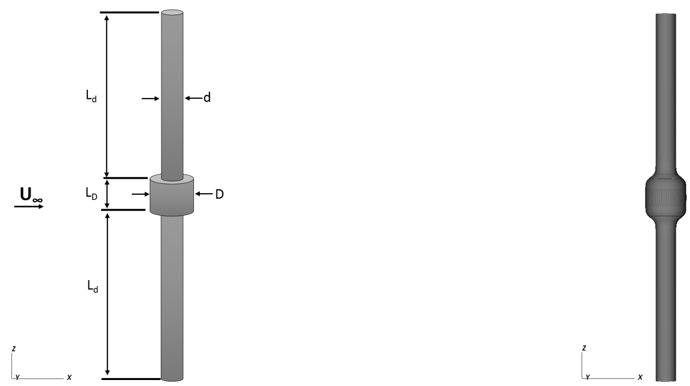

(a) (b)

Figure 9: Sketch of the dual-step cylinder under investigation. Figure (a) is the experimental model of [46] while figure (b) is the current simulation model. d and D represent the small and large diameter, respectively. L_d and L_D are the length of small and large cylinder along the span-wise direction, respectively.

impact of the gradual-change of the radius is negligible compared with the experimental measurements that was carried out on a steep-change cylinder, in terms of the mean flow characteristics. Another difference between the aforementioned experimental works and our simulations is the aspect ratio L_d/d. In the experiment, L_d/d was large enough to make the small cylinder behave similar to an 'infinite' cylinder, e.g., as shown in the table 3, $L_d/d > 15$ [45]. For our SEF-SPM simulation, as shown in section 3, the resolution along the span-wise direction is restricted by the variation of the radius of the cylinder, therefore a larger aspect ratio of the small cylinder requires many more Fourier modes. Fortunately, as suggested in [48] the vortex shedding from a uniform cylinder mounted between end-plates was close to that from an 'infinite' cylinder when the aspect ratio was larger than 7, thus we have used a model with $L_d/d = 8$ in our simulations. Indeed, we have first studied the impact of L_d/d, the results of which will be discussed in the following.

For the simulations of this section, the computational domain has as a size of $[-10\,d, 30\,d] \times [-20\,d, 20\,d]$ with the center of the cylinders located at $(0, 0)$. The mesh has the MESH2 pattern similar to figure 2 (b), consisting of 84 triangles and 3 735 quadrangles. On the $(x - y)$ plane we employed third order Jacobi polynomial ($M = 3$) while along the span-wise direction, $L_z = 18\,d$, we have used 384 Fourier planes. First, we examine the impact of L_d/d. From table 3, we observe that the vortex shedding frequencies St_D,

St_d and drag coefficient C_d vary less than 1% as L_d/d is increased from 8 to 9. Moreover, for the case of $L_d/d = 8$, the difference between the SEF-SPM solution from that of the experimental measurements in [45] is less than 2% for all the coefficients presented in table 3. In the table, we could also observe that the span-averaged *r.m.s.* value of lift coefficient C_L is sensitive to L_d/d when $L_d/d < 7$. However, we can also find in figure 12b that at $L_d/d = 8$ the predicted value C_L is approaching that of a uniform cylinder. Overall, we can conclude that $L_d/d = 8$ is adequate to eliminate the end-plates effect.

Table 3: Flow past a stationary dual-step cylinder at $Re_d = 1\,000$: Strouhal number $St_D = f_D\, d/U_\infty$, where f_D is the vortex shedding frequency due to the large cylinder; Strouhal number $St_d = f_d\, d/U_\infty$, where f_d is vortex shedding frequency due to the small cylinder; C_d is span averaged cross-sectional drag coefficient defined as $\frac{F_d}{\frac{1}{2}U_\infty^2 d}$; C_L is span averaged cross-sectional *root mean square* value of lift coefficient defined as $\frac{F_L}{\frac{1}{2}U_\infty^2 d}$, where F_d and F_L are the drag force and lift force on each cross-section, respectively.

Re_d	Study	L_d/d	St_D	St_d	C_d	C_L
1 050	Morton and Yarusevych [45]	> 15	0.13	0.205	-	-
1 000	SEF-SPM	5	0.135	0.196	1.06	0.027
		8	0.133	0.201	1.03	0.038
		9	0.131	0.202	1.02	0.039
		11	0.132	0.201	1.03	0.043

The instantaneous wake topology of the stationary dual-step cylinder at $Re_d = 1\,000$ is illustrated in figure 10. The pattern of the vortices resembles the experimental visualization of hydrogen bubble presented by Morton and Yarusevych [45]. At the spanwise positions that $|z/d| > 7$, the vortices shed from the small cylinder are almost parallel to the cylinder axis, while at the spanwise positions that $|z/d| < 7$, the vortices from the small cylinder seem to be deformed due to the vortices from the large cylinder; no hairpin-like vortices could be observed in the wake behind the large cylinder. The mean stream-wise velocity on the $y/d = 0$ plane is shown in figure 11. In general, the wake pattern looks very similar to the corresponding PIV image presented in figure 2(b) of [46]. From figure 11, we observe that there is a notable re-circulation bubble both behind the large and small cylinders. In our simulation the re-circulation bubble behind the large cylinder extends

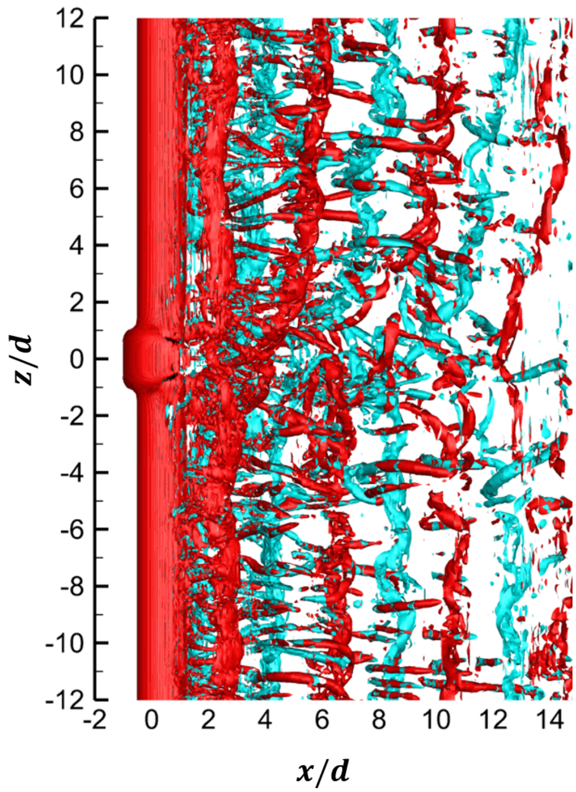

Figure 10: Flow past a stationary dual-step cylinder at $Re_d = 1\,000$: Instantaneous iso-surfaces of $Q = 1$. Red: $\omega_z > 0$; cyan: $\omega_z < 0$. Note we have shifted $z/d = 0$ to the middle of the large cylinder.

about $3.5d$ while in the PIV experiments by Morton et al. [46] it extends approximately $4d$. Figure 12 exhibits the time-averaged C_d and C_L along the cylinder span: blue lines $L_d/d = 12$; red lines $L_d/d = 8$. The magnitude of C_d on the large cylinder is lower than that on small cylinder. We also observe that C_d is symmetric with respect to the midplane ($z/d = 0$). Starting from one end of the cylinder ($|z/d| > 9$), the magnitude of C_d has a constant value around 1.08 until the position $|z/d| \approx 6$. Subsequently, in the range $1.75 \geq |z/d| \geq 3$, the magnitude of C_d deceases rapidly and reaches its minimum value 0.575 at $z/d = 1.75$. However, from $z/d = 1.75$, which is also the starting point of the large cylinder, to $z/d = 0$ the magnitude of C_d increases to 0.84. The span-averaged C_d is about 9% smaller than that of a uniform cylinder. It is noteworthy that drag reduction due to

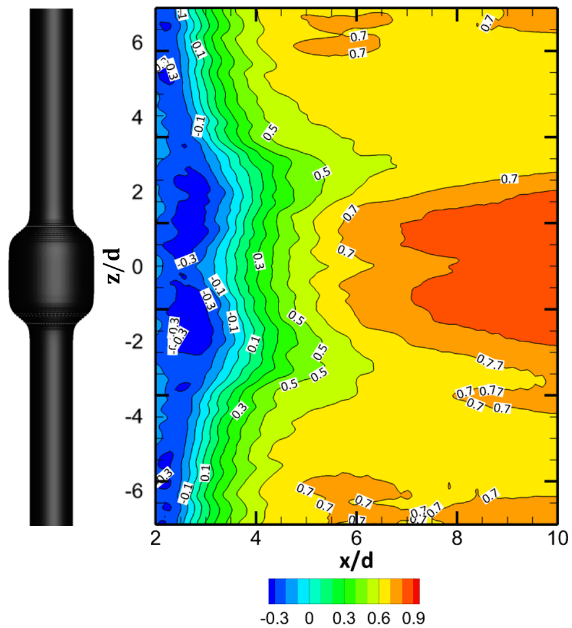

Figure 11: Flow past a stationary dual-step cylinder at $Re_d = 1\,000$: Contours of mean stream-wise velocity u/U_∞ on plane $y = 0$. Note that our simulation result of u/U_∞ resembles the PIV measurements shown in figure 2(b) of [46].

step-cylinder was also reported in [49], who observed 15% reduction in their experimental studies at $Re_D \geq 20\,000$. In figure 12 (b), the time-averaged C_L looks nearly symmetric with respect to the midplane. The magnitude of time-averaged C_L is approaching to the uniform cylinder value only in a range of $|z/d| \geq 8$. It decreases to a minimum 0.026 at $|z/d| \approx 3.2$. In the range of $1.4 \leq |z/d| \leq 3.2$, the magnitude increases to 0.045, while in the subsequent small range $0.8 < |z/d| \leq 1.4$, it decreases again to 0.042. Finally, in the range $|z/d| \leq 0.8$, the magnitude reaches 0.052.

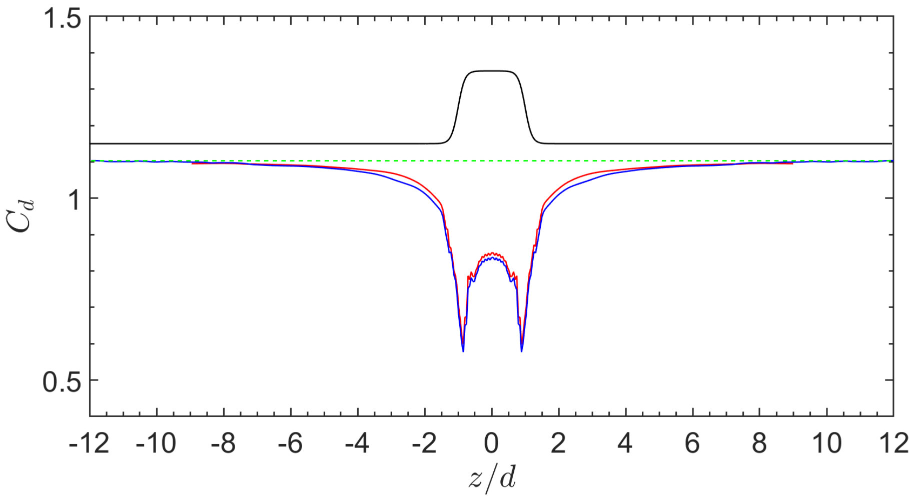

(a)

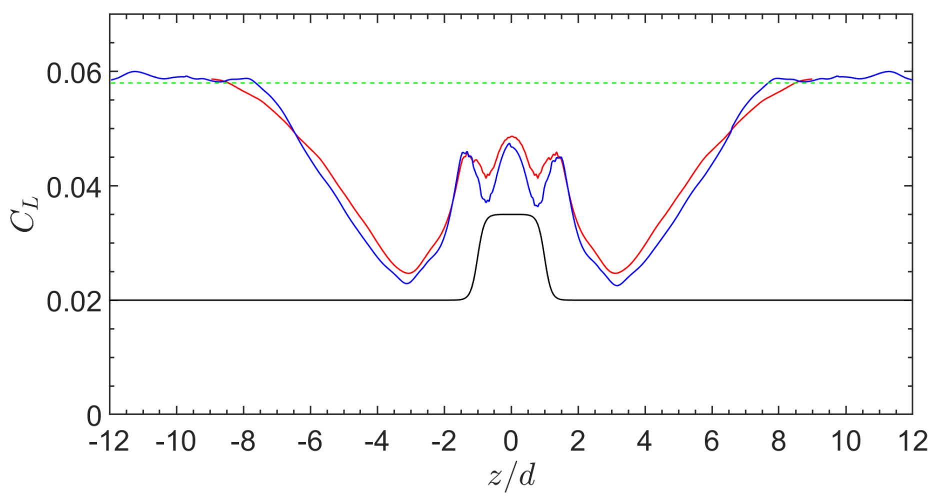

(b)

Figure 12: Flow past a stationary dual-step cylinder at $Re_d = 1\,000$: figure (a) and figure (b) are the time-averaged drag and lift coefficient, respectively. Red line represents the result of $L_d/d = 8$, while blue line represents the result of $L_d/d = 11$. Green dashed horizontal line in figure (a) represents our simulation result of C_D of uniform cylinder at $Re_d = 1,000$, while green dashed horizontal line in figure (b) represents C_L of uniform cylinder at $Re_d = 1,000$ from [3]. Black lines in figure (a) and (b) represent the profile of the radius of the dual-step cylinder along the span (rescaled accordingly). Note we have shifted $z/d = 0$ to the middle of the large cylinder.

4.2. Rigidly moving dual-step cylinder

The simulations of the stationary dual-step cylinder show that there are two frequencies due to the different diameters. In practical offshore application, one of the problem that has been experimentally investigated [50] is which frequency dominates the excitation of the vibration? To address this question, in this section, we study an elastically mounted dual-step cylinder at $Re_d = 1\,000$. For all the simulations herein, the density of the entire dual-step cylinder is assumed to be uniform; the mass per unit length of the small cylinder is $m = 2$, which gives rise to the real mass ratio of the small cylinder be $m \cdot \frac{4}{\pi} \approx 2.55$. The response of the dual-step cylinder is also related to the parameters of the structure. In equation 16, we set $\omega_c = 0$, then we systematically tuned $\omega_b = 2\pi\, f_N$, where $0.094 \leq f_N \leq 0.295$ is the structure natural frequency. Note that according to [14], the modified natural frequency f_N^* is equal to $f_N \sqrt{\frac{m}{m+\frac{\pi}{4}\, C_m}}$, where C_m is the added mass coefficient that is taken equal to 1. As a result, the corresponding f_N^* range is $[0.08, 0.25]$, which leads to the reduced velocity $U^* = \frac{U_\infty}{f_N^*\, d}$ range $[4, 12.5]$. The simulation results of the maximum response amplitude are presented in figure 13. We see that the overall pattern of the response curve with respect to the reduced velocity U^* is quite similar to that of a bare cylinder. One notable difference is that the maximum non-dimensional amplitude in figure 13 is about 0.68, which is smaller than the predicted value 0.73 of bare cylinder, see subsection 3.3. The results of response frequencies and vortex shedding frequencies of the rigidly moving dual-step cylinder are shown in figure 14. We can clearly see that this response is divided into three regimes: A, B and C. In regime A, where $U^* \leq 5.90$, the vortex shedding frequency of the large cylinder is different from that of the small one, and the dual-step cylinder is locked in to the vortex shedding of the small cylinder. In regime B, the response frequency is more complicated: at $U^* = 6.94$, the vortex shedding frequency of the large and small cylinders is the same, but the vibrating frequency is slightly higher than the vortex shedding frequency; in the sub-regime $7.82 \leq U^* \leq 8.74$, both the vortex shedding frequencies and vibrating frequency have the same value. Finally, in regime C, e.g. at $U^* = 10.73$, the vortex shedding frequency of the large cylinder and that of the small cylinder is different, but now the dual-step cylinder is locked in to the vortex shedding of the large cylinder.

In figure 15 we present four power spectral densities (PSD) of the cross-flow velocity time histories that were recorded at two positions: blue line is at $x/d = 3$, $y/d = 0$, $z/d = 4.5$ and red line at $x/d = 3$, $y/d = 0$, $z/d = 9$. The former position is behind the small cylinder while the later is behind the large cylinder. In figure 15(a), $U^* = 4.0$ is in regime A where the system is locked in to the wake of small cylinder; the primary peak of the spectrum of the large cylinder wake is apparently far from that of small cylinder wake. Moreover, we can see that the peak of spectrum of the large cylinder wake is stronger than that of the small cylinder wake, but the system is still locked in to the vortices of the small cylinder. This is because the reduced velocity of the peak frequency of the large cylinder wake based on the large diameter D is 2 ($U^* = \frac{U_\infty}{f_N^* D} = 2$), which is very close to the lower bound of the response regimes in which VIV occurs [51], thus the system of the dual-step cylinder cannot lock in to the large cylinder wake. Increasing the value of U^* to 6.94 in regime B, the magnitude of the peak of the spectrum of the small cylinder wake is much lower than that of the previous case, also the spectrum of the large cylinder wake doesn't exhibit any primary peaks. The weak peak of the spectra reveals the fact that the system is locked in to a frequency that is a little bit higher than the vortex shedding frequencies, i.e. the vibration is not synchronized with the vortex shedding. Further increasing U^* to 7.82 but still in regime B, the two primary peaks coincide and the system is locked in to this peak, as shown in figure 15(c). In figure 15(d), $U^* = 10.73$ that is in regime C, and the primary peak of spectrum of the large cylinder wake is again shifted away from that of the small cylinder. Note that $U^* = 10.73$ is close to the upper bound of the response regime, but the corresponding reduced velocity based on the large diameter $U_D^* = 5.37$, which is in the middle of the response regimes, thus the system of the dual-step cylinder could be locked in to the *large cylinder* vortex shedding. Note that the overall length of the large cylinder is quite small ($L_D/L_d = \frac{1}{9}$, see figure 9), thus it is expected that the response amplitude is smaller than that of the case when the system is locked in to the wake of small cylinder. Moreover, now the secondary peak appears in the spectrum of the small cylinder wake that is induced by the vibration.

In summary, the main finding from the simulations presented in this section is that the dual-step cylinder could either vibrate at the vortex shedding frequency of the large cylinder or the small cylinder, providing that the corresponding reduced velocity based on its own diameter is in the response regimes that is characterized by Khalak and Williamson [51] for uniform rigid cylinder. In particular, for small values of the reduced velocity, the sys-

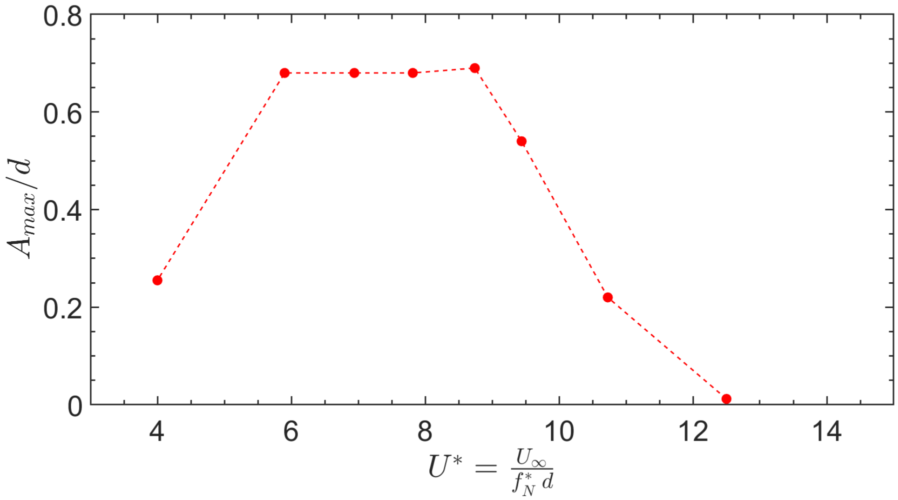

Figure 13: Flow past a self-excited rigidly moving dual-step cylinder at $Re_d = 1\,000$: maximum response amplitude varies with the reduced velocity. $f_N^* = f_N \sqrt{\frac{m}{m+\frac{\pi}{4} C_m}}$ is the modified natural frequency that takes into account the added mass.

tem locks in to the small cylinder frequency. For intermediate values of the reduced velocity, the system locks in to a frequency close to the frequency of the large cylinder. For large values of the reduced velocity, the system locks in to a modified frequency, which is below the frequency of the large cylinder and far from the frequency of the small cylinder.

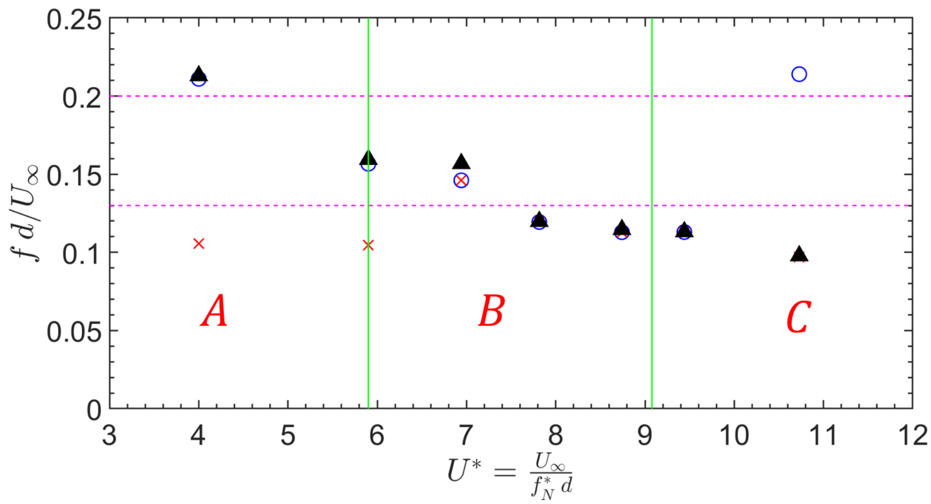

Figure 14: Flow past a self-excited rigidly moving dual-step cylinder at $Re_d = 1\,000$: response frequency and dominant vortex shedding frequencies. Black solid triangle represents the frequency of vibration, blue blank circle is the frequency of vortex shedding from small cylinder, red cross is the frequency of vortex shedding from large cylinder. The pink horizontal dashed lines represent the corresponding vortex shedding frequencies of the stationary small and large cylinders; the green vertical lines divides the plot into three regimes: A, B and C.

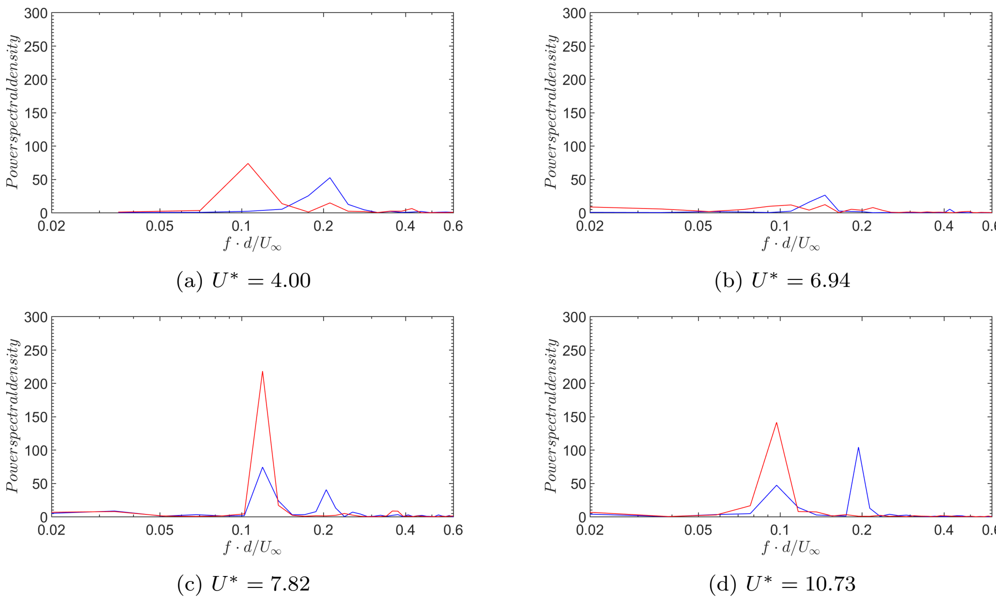

(a) $U^* = 4.00$

(b) $U^* = 6.94$

(c) $U^* = 7.82$

(d) $U^* = 10.73$

Figure 15: Flow past a self-excited rigidly moving dual-step cylinder at $Re_d = 1\,000$: power spectral density of cross-flow velocity at two positions of in near wake. Red line is behind the large cylinder at $x/d = 3, y/d = 0, z/d = 4.5$, blue line is behind the small cylinder at $x/d = 3, y/d = 0, z/d = 2$.

5. Summary

We have presented a robust and flexible method, the spectral-element /Fourier Smoothed Profile Method (SEF-SPM), for simulating VIV problems involving industrial-complexity turbulent flows. Our method has the following attractive properties:

• It is a fast solver for simulating flow past a long riser with complex external surface, e.g., buoyancy module or strakes. SEF-SPM creates a smoothed indicator field by employing a hyperbolic tangent function accounting for the presence of solid-body, which makes Fourier expansion be applicable, hence we can use FFTs.

• It is a robust solver in terms of simulating turbulent flow at high Reynolds number. The entropy-viscosity method (EVM) developed in this paper could efficiently stabilize the simulation that is often under-resolved.

• It is based on a new correlation for the interface thickness parameter ξ that determines the grid resolution. It has a simple linear relationship with the momentum thickness δ_2, and it can be resolved with 2 to 3 grid points. This new correlation is physics-based and is independent of the mesh size and time step. The accuracy of this method is validated by simulation of turbulent flow past a cylinder at Reynolds number up to 10 000.

• It employs a Coordinate Transformation(Mapping method) that significantly reduces the number of mesh cells for VIV problems.

The SEF-SPM simulation of flow past a self-excited rigidly moving dual-step cylinder at $Re_d = 1\,000$ shows that the cylinder could either vibrate at the vortex shedding frequency of the large cylinder or the small cylinder. Currently, our method is being applied to predict the response of a flexible riser with multiple buoyancy modules, in conjunction with ongoing experimental work in [8, 9].

Acknowledgment

The authors gratefully acknowledge support by the Chevron-MIT University Partnership Program and the ESRDC ONR project. The simulations were performed on the parallel cluster of the Center for Computation & Visualization at Brown University.

Appendix A. The study of parameter of α

In equations (6) and (5), $R(\mathrm{u})$ and $E(\mathrm{u})$ have the units that are $\frac{\mathrm{m}^2}{\mathrm{sec}^3}$ and $\frac{\mathrm{m}^2}{\mathrm{sec}^2}$, which are same as that of the turbulence dissipation rate ϵ and turbulence kinetic energy k, respectively, therefore intuitively, we propose the following approximation:

$$\frac{\|R^K_{ijm}(\mathrm{u})\|_{L^\infty(K)}}{\|E^K_{ijm}(\mathrm{u}) - \bar{E}(\mathrm{u})\|_{L^\infty(\Omega)}} \approx C_x \frac{\epsilon}{k}, \tag{A.1}$$

where C_x is a constant. Then by substituting equation (A.1) into equation (4), and assuming that the entropy-viscosity obtained from equation (4) is equal to the eddy viscosity of the Smagorinsky model, we obtain:

$$\alpha C_x \frac{\epsilon}{k} (\delta_K)^2 \approx (\mathrm{C}_s \delta_K)^2 \overline{S}. \tag{A.2}$$

In the above equation, the right-hand-side is the eddy-viscosity of Smagorinsky model, where $\overline{S} = (2\overline{S}_{ij}\,\overline{S}_{ij})$ is defined based on the rate-of-strain tensor, and

$$\mathrm{C}_s = \frac{1}{\pi}\Big(\frac{2}{3\mathrm{C}_K}\Big)^{3/4} \tag{A.3}$$

is the Smagorinsky coefficient, where $\mathrm{C}_K = 1.5$ is the Kolmogorov constant. Equation (A.2) could be simplified as:

$$\alpha \approx \frac{(\mathrm{C}_s)^2}{C_x} \overline{S} \frac{k}{\epsilon}. \tag{A.4}$$

Furthermore, [52] (page 589) gives an estimation that

$$\frac{\big\langle \overline{S}^2 \big\rangle^{1/2} k}{\epsilon} \approx \pi^{2/3} \Big(\frac{3}{2}\mathrm{C}_K\Big)^{1/2} \Big(\frac{\Delta}{L}\Big)^{-2/3}, \tag{A.5}$$

where Δ is a filter width and $L = k^{3/2}/\epsilon$ is the flow lengthscale. Note that in above equation we assume $\big\langle \overline{S}^2 \big\rangle^{1/2} \approx \overline{S}$. By substituting equations (A.3), (A.5) into equation (A.4), we obtain,

$$\alpha = \Big(\frac{3}{2} C_K C_x\Big)^{-1} \pi^{-4/3} \Big(\frac{\Delta}{L}\Big)^{-2/3}. \tag{A.6}$$

In equation A.6, the constants $\frac{\Delta}{L}$ and C_x need to estimate.

First of all, [52] (page 187) writes that the lengthscale splitting the inertial subrange and energy-containing range is defined as $L_{EI} = \frac{1}{6}L$. Moreover, [52] (page 560) recommends that for LES, the filter width Δ should be fine enough to resolve 80% of the energy, which corresponds to the following estimation [52] (page 577),

$$\frac{\Delta}{L} = \frac{1}{12}. \tag{A.7}$$

Next, in particular, if we assume $C_x = 1$, we could obtain a specific value for α:

$$\alpha \approx 0.5. \tag{A.8}$$

Here we study the impact of parameter α by simulating flow past a stationary cylinder at $Re = 10\,000$. Table A.4 shows that $-C_p$ and C_D increase as α increases, and the length of re-circulation bubble behind the cylinder decreases. It is noteworthy that the results at $\alpha = 0.5$ agree better with that of DNS of [39]. Examining the distribution of Cp on the surface of the cylinder in figure A.16, we can observe that the separation angle barely changed when α is changed from 0.5 to 0.05, but there is notable decreasing of C_p behind the separation point. Figure A.17 presents the cross-flow velocity spectrum at a location that $x/d = 3.0$, $y/d = 0.0$. It could be observed that both simulations at $\alpha = 0.5$ and $\alpha = 0.05$ could accurately capture the primary and secondary peaks, but as expected, the spectrum at $\alpha = 0.5$ exhibits more diffusion than that of $\alpha = 0.05$.

To summarize, for EVM simulation of turbulent flow past a cylinder, $\alpha = 0.5$ leads to best prediction in terms of mean flow characteristics.

Table A.4: Flow past a stationary cylinder at $Re = 10\,000$: pressure ($-C_P$) and drag (C_D) coefficients, Strouhal number (St), and length of the separation bubble (L_r). DNS values are from [39]

Re	**study**	$\boldsymbol{\alpha}$	$\boldsymbol{p}$	$\boldsymbol{C_D}$	$\boldsymbol{-C_P}$	$\boldsymbol{St}$	$\boldsymbol{L_r}$
$\mathbf{10^4}$	SEF-SPM	0.5	64	1.239	1.196	0.196	0.93
			128	**1.151**	**1.024**	**0.196**	**0.98**
		0.25	64	1.292	1.251	0.197	0.82
			128	1.209	1.086	0.198	0.88
		0.05	64	1.410	1.379	0.197	0.65
			128	1.324	1.278	0.199	0.78
	DNS	-	**128**	**1.143**	**1.129**	**0.203**	**0.82**

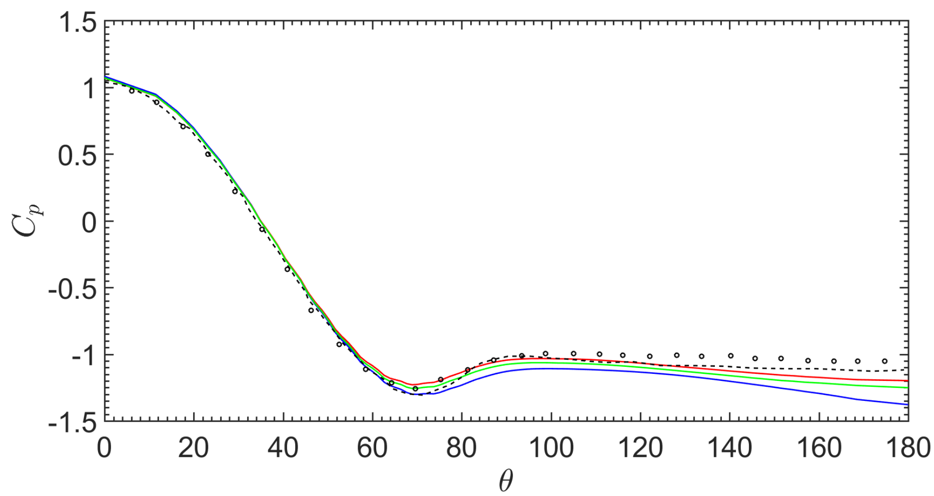

Figure A.16: Flow past a stationary cylinder at $Re = 10\,000$: pressure coefficient along the surface of the cylinder. Red line, SEF-SPM solution at $\alpha = 0.5$; green line, SEF-SPM solution at $\alpha = 0.05$; blue line, SEF-SPM solution at $\alpha = 0.05$; black circles, experimental measurements of Norberg [43] at $Re = 8\,000$; black dashed line, high resolution DNS of Dong et al. [39] at $Re = 10\,000$. Note here SEF-SPM employs 64 Fourier planes.

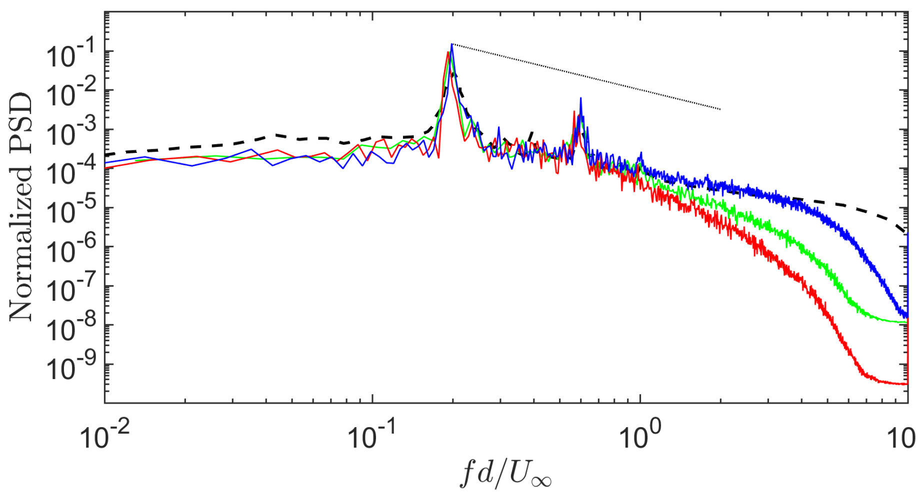

Figure A.17: Flow past a stationary cylinder at $Re = 10\,000$: cross-flow velocity spectra at $x/d = 3.0$, $y/d = 0$. Red line, SEF-SPM solution at $\alpha = 0.5$; green line SEF-SPM solution at $\alpha = 0.25$; blue line, SEF-SPM solution at $\alpha = 0.05$. black dashed line is DNS of Dong et al. [39] at the point that $x/d = 3.01$, $y/d = 0.38$; black dotted line is the $-\frac{5}{3}$ power law. Note here SEF-SPM employs 64 Fourier planes.

[1] G. Gerrard, The wakes of cylindrical bluff bodies at low Reynolds number, Philosophical Transactions of the Royal Society A 288 (1978) 351–382.

[2] C. H. K. Williamson, Vortex dynamics in the cylinder wake, Annual Review of Fluid Mechanics 28 (1996) 477–539.

[3] C. Norberg, Fluctuating lift on a circular cylinder: review and new measurements., Journal of Fluids and Structures 17 (2003) 57–96.

[4] C. H. K. Williamson, R. Govardhan, Vortex-induced vibration, Annual Review of Fluid Mechanics 36 (2004) 413–455.

[5] M. S. Triantafyllou, R. Bourguet, J. M. Dahl, Y. Modarres-Sadeghi, Vortex induced vibration, Springer International Publishing, London, UK, 2016.

[6] S. Holmes, J. O. H. Oakley, Y. Constantinides, Simulation of riser VIV using fully three dimensional CFD simulations, in: 25th International Conference on Offshore Mechanics and Arctic Engineering, ASME, Hamburg, Germany, 2006.

[7] Y. Constantinides, M. Zhang, VIV assessment of deepwater lazy-wave risers, in: 33rd International Conference on Ocean, Offshore and Arctic Engineering, ASME, 2014.

[8] J. L. Garrec, D. Fan, B. Wu, M. S. Triantafyllou, Experimental investigation of cross flow - inline coupled Vortex-Induced Vibration on riser with finite length buoyancy module, in: OCEANS 2016 MTS/IEEE Monterey, 2016.

[9] D. Fan, M. S. Triantafyllou, Vortex Induced Vibration of Riser with Low Span to Diameter Ratio Buoyancy Modules, in: The 27th International Ocean and Polar Engineering Conference, 2017.

[10] G. E. Karniadakis, Spectral element-Fourier methods for incompressible turbulent flows., Computer Methods in Applied Mechanics and Engineering 80 (1990) 367–380.

[11] D. J. Newman, G. E. Karniadakis, A direct numerical simulation study of flow past a freely vibrating cable, Journal of Fluid Mechanics 344 (1997) 95–136.

[12] C. Evangelinos, G. E. Karniadakis, Dynamics and flow structures in the turbulent wake of rigid and flexible cylinders subject to vortex-induced vibrations, Journal of Fluid Mechanics 400 (1999) 91–124.

[13] D. Lucor, L. Imas, G. E. Karniadakis, Vortex dislocations and force distribution of long flexible cylinders subjected to sheared flows, Journal of Fluids and Structures 15 (2001) 641–650.

[14] R. Bourguet, G. E. Karniadakis, M. S. Triantafyllou, Vortex-induced vibrations of a long flexible cylinder in shear flow, Journal of Fluid Mechanics 677 (2011) 342–382.

[15] Y. Nakayama, R. Yamamoto, Simulation method to resolve hydrodynamic interactions in colloidal dispersions, Physical Review E 71 (2005) 036707.

[16] R. Yamamoto, K. Kim, Y. Nakayama, Strict simulations of non-equilibrium dynamics of colloids, Colloids and Surfaces A: Physicochemical and Engineering Aspects 311 (2007) 42–47.

[17] R. Yamamoto, Smoothed Profile method to simulate colloidal particles in complex fluids, International Journal of Modern Physics C 20 (2009) 1457–1465.

[18] T. Iwashita, Y. Nakayama, R. Yamamoto, A Numerical Model for Brownian Particles Fluctuating in Incompressible Fluids, Journal of the Physical Society of Japan 77 (2008) 074007.

[19] A. Hamid, R. Yamamoto, Direct numerical simulations of anisotropic diffusion of spherical particles in sedimentation, Physical Review E 87 (2013) 022310.

[20] X. Luo, M. R. Maxey, G. E. Karniadakis, Smoothed profile method for particulate flows: error analysis and simulations, Journal of Computational Physics 228 (2009) 1750–1769.

[21] X. Luo, A. Beskok, G. E. Karniadakis, Modeling electrokinetic flows by the smoothed profile method, Journal of Computational Physics 229 (2010) 3828–3847.

[22] S. Kang, Y. K. Suh, Direct simulation of flows with suspended paramagnetic particles using one-stage smoothed profile method, Journal of Fluids and Structures 27 (2011) 266–282.

[23] F. Mohaghegh, H. S. Udaykumar, Comparison of sharp and smoothed interface methods for simulation of particulate flows I: Fluid structure interaction for moderate Reynolds numbers, Computers and Fluids 140 (2016) 39–58.

[24] F. Mohaghegh, H. S. Udaykumar, Comparison of sharp and smoothed interface methods for simulation of particulate flows II: Inertial and added mass effects, Computers and Fluids 143 (2017) 103–119.

[25] F. Romanó, H. C. Kuhlmann, Smoothed-profile method for momentum and heat transfer in particulate flow, International Journal for Numerical Methods in Fluids 83 (2017) 485–512.

[26] M. Zayernouri, S. W. Park, D. M. Tartakovsky, G. E. Karniadakis, Stochastic smoothed profile method for modeling random roughness in flow problems, Computer Methods in Applied Mechanics and Engineering 23 (2013) 99–112.

[27] X. Luo, B. Epps, C. Chryssostomidis, G. E. Karniadakis, Comparison of Turbulence Models for Simulating Flow in Waterjets, in: 11th International Conference on Fast Sea Transportation, Honolulu, Hawaii, USA, 2011.

[28] J. Guermond, R. Pasquetti, B. Popov, From suitable weak solutions to entropy viscosity, Journal of Scientific Computing 49 (1) (2011) 35–50.

[29] J. L. Guermond, R. Pasquetti, B. Popov, Entropy viscosity method for nonlinear conservation law, Journal of Computational Physics 230 (11) (2011) 4248–4267.

[30] J. L. Guermond, A. Larios, T. Thompson, Validation of an entropy-viscosity model for large eddy simulation, J. Fröhlich, H. Kuerten, B.J. Geurts, V. Armenio (Eds.), Direct and large-eddy simulation IX, ERCOFTAC series 20 (2015) 43—48.

[31] Z. Wang, M. S. Triantafyllou, Y. Constantinides, G. E. Karniadakis, An entropy-viscosity LES study of turbulent flow in a flexible pipe, Submitted to Journal of Fluid Mechanics .

[32] G. E. Karniadakis, S. Sherwin, Spectral/hp Element Methods for Computational Fluid Dynamics, 2nd edition, Oxford University Press, Oxford,UK, 2005.

[33] T. Warburton, Spectral/hp element methods on polymorphic multi-domains: Algorithms and applications, Ph.D. thesis, Brown University, 1998.

[34] H. Schlichting, K. Gersten, Boundary-Layer Theory, Springer, ninth edition edn., 2017.

[35] A. G. Tomboulides, S. A. Orszag, Numerical investigation of transitional and weak turbulent flow past a sphere, Journal of Fluid Mechanics 416 (2000) 45–73.

[36] T. A. Johnson, V. C. Patel, Flow past a sphere up to a Reynolds number of 300, Journal of Fluid Mechanics 378 (1999) 19–70.

[37] J. Yang, E. Balaras, Parallel large-eddy simulations of turbulent flows with complex moving boundaries on fixed Cartesian grids, in: Parallel Computational Fluid Dynamics 2005, Theory and Applications, 101–108, 2006.

[38] R. D. Henderson, Details of the drag curve near the onset of vortex shedding, Physics of Fluids 7 (9) (1995) 2102–2104.

[39] S. Dong, G. E. Karniadakis, A. Ekmekci, D. Rockwell, A combined direct numerical simulation-particle image velocimetry study of the turbulent near wake, Journal of Fluid Mechnics 569 (2006) 185–207.

[40] A. G. Kravchenko, P. Moin, Numerical studies of flow over a cicular cylinder at ReD = 3900., Physics of Fluids 12 (403–417).

[41] P. Parnaudeau, J. Carlier, D. Heitz, E. Lamballais, Experimental and numerical studies if the flow over a circular cylinder at Reynolds number 3900, Physics of Fluids 20 (2008) 085101.

[42] L. M. Lourenco, C. Shih, Characteristics of the plane turbulent near wake of a circular cylinder, a particle image velocimetry study (data taken from Beaudan & Moin 1994).

[43] C. Norberg, Pressure forces on a circular cylinder in cross flow, in: H. Eckelmann, J. Graham, P. Huerre, P. Monkewitz (Eds.), Proceedings of IUTAM Symposium on Bluff-Body Wakes, Dynamics and Instabilities, Springer-Verlag, Berlin, 275–278, 1993.

[44] C. Morton, S. Yarusevych, An experimental investigation of flow past a dual step cylinder, Experiments in Fluids 1 (2012) 69–83.

[45] C. Morton, S. Yarusevych, On vortex shedding from low aspect ratio dual step cylinders, Journal of Fluids and Structures 44 (2014) 251–269.

[46] C. Morton, S. Yarusevych, F. Scarano, A tomographic particle imgae velocimetry investigation of the flow development over dual step cylinders, Physics of Fluids 28 (2016) 025104.

[47] J. McClure, C. Morton, S. Yarusevych, Flow development and structural loading on dual step cylinders in laminar, Physics of Fluids 27 (2015) 063602.

[48] C. Norberg, An experimental investigation of the flow around a circular cylinder: influence of aspect ratio., Journal of Fluid Mechanics 258 (1994) 287–316.

[49] H. Nakamura, T. Igarashi, Omnidirectional reductions in drag and fluctuating forces for a circular cylinder by attaching rings, Journal of Wind Engineering & Industrial Aerodynamics 96 (2008) 887–899.

[50] Z. Rao, J. K. Vandiver, V. Jhingran, VIV Excitation competition between bare and bouyant segments of flexible cylinders, in: Proceedings of the ASME 32nd International Conference on Ofshore Mechanics and Arctic Engineering, 2013.

[51] A. Khalak, C. H. K. Williamson, Motions, forces and modes transitions in vortex-induced vibration at low mass-damping, Journal of Fluids and Structures 13 (1999) 813–851.

[52] S. B. Pope, Turbulent Flows, Cambridge University Press, New York, 2000.